

# Joint estimation of a two-phase spin rotation beyond classical limit

Jiahao Cao,<sup>1,2</sup> Xinwei Li,<sup>3,\*</sup> Tianwei Mao,<sup>1</sup> Wenxin Xu,<sup>1</sup> and Li You<sup>1,2,4,5,6,†</sup>

<sup>1</sup>*State Key Laboratory of Low Dimensional Quantum Physics,  
Department of Physics, Tsinghua University, Beijing 100084, China*

<sup>2</sup>*Beijing Academy of Quantum Information Sciences, Beijing 100193, China*

<sup>3</sup>*Graduate School of China Academy of Engineering Physics, Beijing 100193, P. R. China*

<sup>4</sup>*Frontier Science Center for Quantum Information, Beijing, China*

<sup>5</sup>*Collaborative Innovation Center of Quantum Matter, Beijing 100084, China*

<sup>6</sup>*Hefei National Laboratory, Hefei, Anhui 230088, China*

(Dated: December 19, 2023)

Quantum metrology employs entanglement to enhance measurement precision [1–3]. The focus and progress so far have primarily centered on estimating a single parameter. In diverse application scenarios, the estimation of more than one single parameter is often required. Joint estimation of multiple parameters can benefit from additional advantages for further enhanced precision. Here we report quantum-enhanced measurement of simultaneous spin rotations around two orthogonal axes, making use of spin-nematic squeezing in an atomic Bose-Einstein condensate. Aided by the  $F = 2$  atomic ground hyperfine manifold coupled to the nematic-squeezed  $F = 1$  states as an auxiliary field through a sequence of microwave (MW) pulses, simultaneous measurement of multiple spin-1 observables is demonstrated, reaching an enhancement of 3.3 to 6.3 decibels (dB) beyond the classical limit over a wide range of rotation angles. Our work realizes the first enhanced multi-parameter estimation using entangled massive particles as a probe. The techniques developed and the protocols implemented also highlight the application of two-mode squeezed vacuum states in quantum-enhanced sensing of noncommuting spin rotations simultaneously.

Quantum-enhanced metrology improves parameter estimation precision in sensing beyond the standard quantum limit (SQL), or the classical limit [1–3]. The fruitful recent achievement at advanced LIGO with squeezed light [4], yielding an increased number of events detected [5], has made quantum-enhanced metrology one of the most promising quantum technologies in the near future. It has been demonstrated in experiments with photons [6], neutral atoms [7, 8], trapped ions [9, 10] and artificial atoms [11]. Implemented at high-sensitivity atom interferometers, such as atomic clocks [12] and atomic magnetometers [13], significant technological gains will likely occur soon.

Ideas for quantum-enhanced sensing have been extended to multi-parameter settings as well, where estimations of multiple parameters can simultaneously reach beyond SQL with suitable quantum entanglement [14, 15]. These extensions are relevant for a broad range of applications, such as imaging and microscopy [16, 17], multi-dimensional field sensing [18, 19], and quantum networks for atomic clocks [20] etc., and they have motivated growing interests from both theoretical and experimental perspectives. A significant challenge in multi-parameter estimation arises when the generators of parameter-encoding transformations do not commute. Observables that provide maximal information about different parameters need not necessarily commute [21], which could potentially impair quantum-enhanced sensitivities for all the parameters. Recently, Lorcán O. Conlon, et al. have experimentally demonstrated optimal single- and two-copy collective measurements for simultaneously estimating two noncommuting qubit rotations [22]. On the other

hand, a two-mode Einstein-Podolsky-Rosen (EPR) entangled system exhibits perfect correlations not only between the positions but also between their momenta. For example, the difference  $x_1 - x_2$  of the position operators  $x_1$  and  $x_2$  commutes with the sum  $p_1 + p_2$  of the momentum operators  $p_1$  and  $p_2$ , likewise for  $x_1 + x_2$  and  $p_1 - p_2$ . Such EPR correlation is known to be capable of exhibiting squeezed noise in two conjugate observables, which allows for the simultaneous estimation of two encoded parameters beyond the classical limit. The original idea was first delineated in the form of quantum dense coding [23] and was later demonstrated experimentally with optical parametric amplifiers [24–27]. A related recent study [28] reports estimating displacements beyond the SQL along two quadratures for the center-of-mass motion of a trapped ion. We also notice that a two-mode squeezed state can be also prepared with trapped ion system with a laser-free method using additional radio potentials, which is utilized to demonstrate the SU(1,1) interferometers [29].

The quantum-enhanced joint estimation we report concerns a spin rotation characterized by two unknown phases encoded into noncommuting collective spin components  $L_x$  and  $L_y$  of a spinor atomic Bose-Einstein condensate (BEC). The EPR-like entanglement is revealed to be inherent in the spin-nematic squeezed state generated by atomic spin-mixing [30–32], which is found to exhibit squeezed quantum noise in both spin-nematic SU(2) subspaces [33]. The associated correlation is demonstrated experimentally capable of beating the SQL precision by joint estimation of the two rotation phases simultaneously in this work. To read out the phases encoded

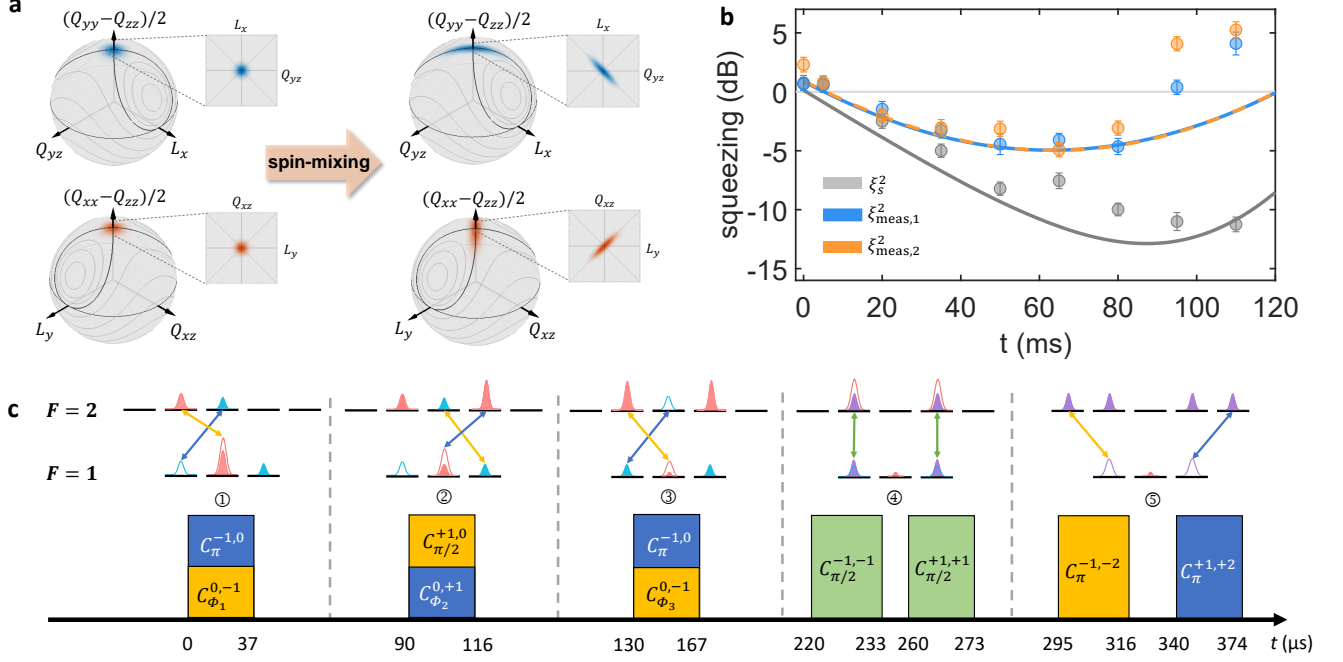


FIG. 1. Spin-nematic squeezing in both SU(2) subspaces. (a) The generation of spin-nematic squeezed state is illustrated by quasi-probability distributions on both SU(2) subspace Bloch spheres, respectively spanned by  $\{L_y, Q_{xz}, (Q_{xx} - Q_{zz})/2\}$  and  $\{Q_{yz}, L_x, (Q_{yy} - Q_{zz})/2\}$ , simulated here for  $N = 100$  atoms. The initial polar state corresponds to all atoms in the  $m_F = 0$  component. After a short evolution time at  $q \approx |c_2|$ , spin-nematic squeezing develops along the separatrix (dark gray lines) on both Bloch spheres. (b) The measured squeezing parameter at the optimal squeezing (for  $q = |c_2|$ ) versus evolution time. The gray dots show the experimental results of measured squeezing in a single SU(2) subspace by applying an RF rotation to couple sublevels in the  $F = 1$  manifold [31]. The blue and orange dots show the experimental results of simultaneously measured squeezing in both SU(2) subspaces by the MW pulse sequence using the  $F = 2$  manifold as an ancillary field. The squeezing parameter of the simultaneous measurement scheme diminishes at longer times due to imperfections of the MW pulses as well as other decoherence or dissipation mechanisms. All markers denote experimental results averaged over 100 runs and the corresponding solid and dashed lines denote numerical calculations based on truncated Wigner approximation. (c) The lower panel shows the MW pulse measurement sequence. The complete measurement scheme lasts for about 374  $\mu\text{s}$  in a single experiment run. The blue, yellow, and green squares correspond to the MW pulses with  $\sigma_+$ ,  $\sigma_-$ , and  $\pi$ -polarization, respectively. The upper panel illustrates atom number distributions in all sublevels before (empty shape) and after (filled shape) the MW pulse is implemented. The blue and red shapes denote the signals and pump fields for atomic homodyne detection, while the purple shapes depict the atoms after  $\pi/2$ -pulse couplings between the signals and the pumps. A small number of atoms remain in the  $|F = 1, m_F = 0\rangle$  state due to due to imperfections of the pulse sequences. Here  $C_\Phi^{i,j}$  denotes the coherent coupling between  $|F = 1, m_F = i\rangle$  and  $|F = 2, m_F = j\rangle$  at a rotation angle  $\Phi$ . For the first three pulses,  $\Phi_1, \Phi_2$ , and  $\Phi_3$  are adjusted by changing the power ratio between  $\sigma_+$  and  $\sigma_-$  polarizations to approximately split the atoms in  $|F = 1, m_F = 0\rangle$  into two halves coherently.

into the probe state, we implement a protocol to measure the two noncommuting rank-2 quadrupole moments  $Q_{xz}$  and  $Q_{yz}$  of the collective spin observables simultaneously, reminiscent of atomic homodyne detection [30], by taking the  $F = 2$  hyperfine states as the auxiliary ones and applying a sequence of microwave pulses to transform  $Q_{xz}$  and  $Q_{yz}$  into the population differences of atomic hyperfine sublevels while preserving the squeezed noise correlation. With the protocol to be detailed later, both  $Q_{xz}$  and  $Q_{yz}$  are measured in a single experimental run, and the metrological gains for joint estimation of the two phases reach 3.3 dB to 6.3 dB beyond the SQL over a wide range of rotations explored, where the SQL  $1/\sqrt{2N}$  is for

estimating two parameters with an ensemble of  $N$  spin-1 particles [34] (see Supplementary Material). Consistent with the standard practice of estimating a single parameter beyond the classical limit, we carry out strong (collapsing) measurements to obtain the maximal amount of information by adopting an atomic homodyne protocol. In Ref. [35], the back actions on the state for weak continuous measurement of noncommuting observables are studied.

The experimental system is a spinor atomic BEC in the  $F = 1$  ground hyperfine manifold. Under the single spatial mode approximation, it can be described by the

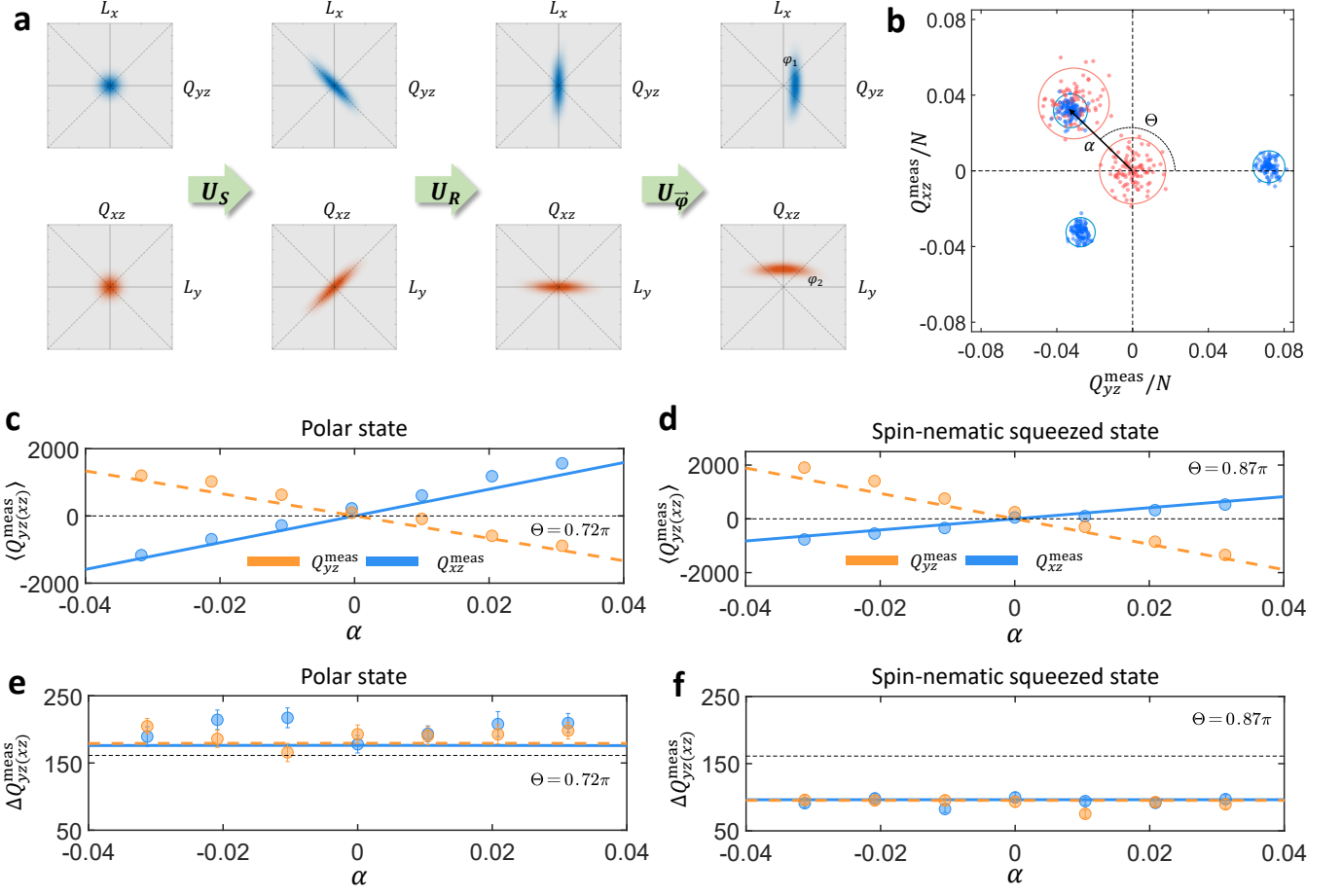


FIG. 2. Joint estimation of spin rotation angles around  $\hat{L}_x$  and  $\hat{L}_y$ . (a) Schematic of the joint estimation interferometry protocol with quasiprobability distributions for the respective states plotted in the  $\{L_x, Q_{yz}\}$  and  $\{L_y, Q_{xz}\}$  planes.  $U_S$ ,  $U_R$ , and  $U_{\vec{\varphi}}$  denote the unitary evolutions generated by spin-mixing, spinor phase rotation, and encoding spin rotations, respectively. (b) The distributions of the simultaneously measured data for the polar state (red dots) and spin-nematic squeezed state (blue dots) sampled over 100 times after spin rotations at different  $\varphi_1$  and  $\varphi_2$  encoded. The distribution of the polar state is much broader than that of the spin-nematic squeezed state, hence the higher sensitivities for the estimation from the latter. Here  $\varphi_1 = \alpha \cos \Theta$  and  $\varphi_2 = \alpha \sin \Theta$ . The red (blue) circles delineate the boundary of the measured data,  $Q_{yz}^{\text{meas}}$  and  $Q_{xz}^{\text{meas}}$ , for the polar (spin-nematic squeezed) state. Each circle is centered at  $(\langle Q_{yz}^{\text{meas}} \rangle / N, \langle Q_{xz}^{\text{meas}} \rangle / N)$ , with a radius of  $\sqrt{3} \sqrt{(\Delta Q_{yz}^{\text{meas}})^2 + (\Delta Q_{xz}^{\text{meas}})^2} / N$ . (c-f) The mean values and standard deviations of the measured  $Q_{xz}$  and  $Q_{yz}$  at variable  $\alpha$  with fixed  $\Theta$  for the polar state (c,e) and spin-nematic squeezed state (d,f) as the probes. Each point represents the average of 100 repeated experiments.

Hamiltonian [36]

$$H = \frac{c_2}{2N} [2(a_1^\dagger a_{-1}^\dagger a_0 a_0 + \text{h.c.}) + (2N_0 - 1)(N - N_0)] - qN_0, \quad (1)$$

with  $a_{m_F}$  and  $a_{m_F}^\dagger$  the creation and annihilation operators for the  $|F=1, m_F = \{0, \pm 1\}\rangle$  component. This Hamiltonian contains an interaction part and a quadratic Zeeman part. The first part includes a spin-mixing term generating paired atoms into  $|F=1, m_F = \pm 1\rangle$  from  $|F=1, m_F = 0\rangle$  and vice versa at a rate of  $|c_2|$ , and an energy shift term caused by elastic collisions. The second part is proportional to the atomic number operator  $N_0$  and the coefficient  $q$  is tunable by a bias magnetic field or an off-resonant MW dressing field [37].

For a condensate prepared initially in the  $|F=1, m_F = 0\rangle$  state or the polar state, nearly all atoms remain in the  $|F=1, m_F = 0\rangle$  state during the short-term spin-mixing dynamics. In this undepleted pump regime, the total number of transferred atoms in  $|F=1, m_F = \pm 1\rangle$  is small, the operator  $a_0$  ( $a_0^\dagger$ ) can be replaced approximately by a complex number  $\sqrt{N}e^{-i\phi}$  ( $\sqrt{N}e^{i\phi}$ ), and the above Hamiltonian reduces to the form of parametric down-conversion

$$H = c_2(e^{-2i\phi} a_1^\dagger a_{-1}^\dagger + \text{h.c.}), \quad (2)$$

when  $q$  is adjusted to compensate for the energy shift of the elastic collision at  $q = |c_2|$ . The interaction Eq. (2) produces a spin-nematic squeezed state as shown

in Fig. 1(a), analog to the two-mode squeezed vacuum state [30, 31] in the widely discussed SU(1,1) interferometry. The sign of Eq. (2) can be easily flipped by inducing a  $\pi$  phase shift of the  $|F = 1, m_F = 0\rangle$  component to realize time-reversed evolution [38]. In this work, we demonstrate that the spin-nematic squeezed state, the atomic analog of the two-mode squeezed vacuum state, is sensitive to the spin rotation transformation  $e^{-i(\varphi_1 L_x + \varphi_2 L_y)}$  parameterized by two phases  $\varphi_1$  and  $\varphi_2$ .

A complete description of the spin-1 system is provided by the SU(3) Cartesian dipole-quadrupole basis, which consists of the three components of the spin operators  $L_i$  and the moments of the rank-2 quadrupoles or nematic tensors  $Q_{ij} = L_i L_j + L_j L_i - (4/3)\delta_{ij}$ , with  $\{i, j\} \in \{x, y, z\}$  and  $\delta_{ij}$  the Kronecker delta notation. In the undepleted pump regime,  $N_0 \sim N$ , the collective spin operator  $L_x$  ( $L_y$ ) and the nematic operator  $Q_{yz}$  ( $Q_{xz}$ ) reduce to  $e^{-i\phi}\sqrt{N}a_S^\dagger + \text{h.c.}$  ( $-ie^{-i\phi}\sqrt{N}a_A^\dagger + \text{h.c.}$ ) and  $-ie^{-i\phi}\sqrt{N}a_S^\dagger + \text{h.c.}$  ( $e^{-i\phi}\sqrt{N}a_A^\dagger + \text{h.c.}$ ) approximately, which are proportional to the quadrature operators of the symmetric and asymmetric superpositions  $a_S^\dagger = (a_1^\dagger + a_{-1}^\dagger)/\sqrt{2}$  and  $a_A^\dagger = (a_1^\dagger - a_{-1}^\dagger)/\sqrt{2}$  of bosonic operators  $a_1^\dagger$  and  $a_{-1}^\dagger$ , respectively.

To read out the parameters  $\varphi_1$  and  $\varphi_2$ ,  $Q_{yz}$  and  $Q_{xz}$  need to be measured simultaneously, i.e., within one experimental run. For the measurement of quadrature operators of electromagnetic fields, homodyne detection represents a successful approach and is implemented by mixing the signal field to the coherent pump field [39]. Here in the spin-1 BEC system, atoms in  $|F = 1, m_F = 0\rangle$  can be treated as a coherent pump field reference in measurements of the equivalent quadrature operators  $Q_{yz}$  and  $Q_{xz}$  [30, 40]. To realize such simultaneous readout,  $\pi/2$  coupling is applied between  $a_1$  and  $a_{-1}$  to form  $a_S$  and  $a_A$ . Additionally, atoms in  $|F = 1, m_F = 0\rangle$  are splitted into two coherent fields, through a tailored sequence of MW pulses with two orthogonal polarizations, which facilitate the coupling between  $F = 1$  manifold and the ancillary states within the  $F = 2$  manifold. This sequence leads to the transformations  $a_{1,1} \rightarrow a_S$ ,  $a_{1,-1} \rightarrow a_A$ , and  $a_{2,\pm 1} \rightarrow a_0/\sqrt{2}$ . To avoid possible confusion with the state index in the above, the full label  $\{F, m_F\}$  for the component mode is adopted here as opposed to the shorthand indexing by  $m_F$  alone in the  $F = 1$  manifold.

The above seemingly cumbersome MW sequence is due to the limitations of our experimental setup, as we were unable to generate a microwave signal that was purely  $\sigma_+$  or  $\sigma_-$  polarized. Consequently, the  $\pi/2$  coupling between  $a_{1,1}$  and  $a_{1,-1}$ , as well as the redistribution of the atoms in  $|F = 1, m_F = 0\rangle$  to the ancillary  $|F = 2, m_F = \pm 1\rangle$  is achieved through the application of the first three MW pulses shown in Fig. 1(c) by adjusting the power ratio between  $\sigma_+$  and  $\sigma_-$  polarizations. These transformations are to be implemented with high fidelity, the rel-

ative strength between  $\sigma_-$  and  $\sigma_+$  polarizations needs to be well controlled. The next two steps mix  $a_S$  and  $a_A$  to the pump mode and transfer the mode quadratures to the atomic population difference  $N_{2,\pm 2} - N_{2,\pm 1}$ . In the end, the read-out phase of the quadrature operators is determined by the phases of the second pulse and the pulses mixing  $a_S$  ( $a_A$ ) to the pump mode.

Our experiment starts with a BEC containing  $N = 26500 \pm 250$   $^{87}\text{Rb}$  atoms in the  $|F = 1, m_F = 0\rangle$  state under a bias magnetic field of 0.828 G and confined in a crossed dipole trap at  $c_2 = -2\pi \times 3.8$  Hz. The effective QZS  $q = q_B + q_{\text{MW}}$  includes contributions from both the bias magnetic field ( $q_B$ ) and a blue-detuned microwave dressing field ( $q_{\text{MW}}$ ) which offers fast and precise control of  $q$ . The spin-mixing dynamics are initiated by quenching  $q$  from  $q \sim 13|c_2|$  to  $q = |c_2|$  through adjusting the power of the dressing microwave. After a short time evolution, a spin-nematic squeezed state is generated and is followed by a  $\pi/4$  spinor phase rotation around the  $(Q_{yy} - Q_{zz})/2$  and  $(Q_{xx} - Q_{zz})/2$  axis simultaneously, effected by two resonant microwave pulses between  $|1, 0\rangle$  and  $|2, 0\rangle$  with  $\pi/4$  phase difference. The quadrature angle of optimal squeezing is then aligned to be most sensitively detected by  $Q_{yz}$  and  $Q_{xz}$ , ensuring the probe state is most sensitive to the two-phase rotation around  $L_x$  and  $L_y$  axes.

As illustrated in Fig. 1(b), spin-nematic squeezing is observed to build up gradually during spin-mixing evolution and the degree of squeezing can be quantified by the parameter

$$\xi^2 = 20 \log_{10} \left( \Delta Q_{yz(xz)} / \sqrt{N} \right). \quad (3)$$

The gray dots show the measured squeezing parameter when only one spin-nematic subspace is detected using the measurement procedure identical to the earlier study [31]. The blue and orange dots illustrate quantum noise reduction in both SU(2) subspaces spanned by  $\{L_y, Q_{xz}, (Q_{xx} - Q_{zz})/2\}$  and  $\{Q_{yz}, L_x, (Q_{yy} - Q_{zz})/2\}$ . The squeezing parameters for the above two should ideally be equal in theory, however, imperfections of the synthesized MW pulses before atom number detection bring in additional noise such as from the fluctuations of signal ( $a_S$  and  $a_A$ ) amplitude and pump ( $a_P$ ) phase (see Supplementary information), which degrades the detected squeezing. For longer evolution times when the system reaches the over-squeezed regime, spin-nematic squeezing parameters measured in both subspaces are found lower due to the breakdown of undepleted pump approximation. The observed squeezing for both  $Q_{xz}$  and  $Q_{yz}$  indirectly benchmark our capability of synthesizing the above MW pulse sequence shown in Fig. 1(c).

The phase encoding operation  $e^{i(\varphi_1 L_x + \varphi_2 L_y)}$  is enacted by small angle RF rotations, which takes about 100  $\mu\text{s}$  to complete. To ensure maximum sensitivity of the probe

state to the phase imprinting procedure, the rotation axis is aligned with the anti-squeezed quadrature as depicted in Fig. 2(a). In the alternatively parameterized form  $\varphi_1 = \alpha \cos \Theta$  and  $\varphi_2 = \alpha \sin \Theta$  as shown in Fig. 2(b),  $\alpha$  of the imprinted phase is controlled experimentally by the duration of the RF pulses while  $\Theta$  by the RF phases.

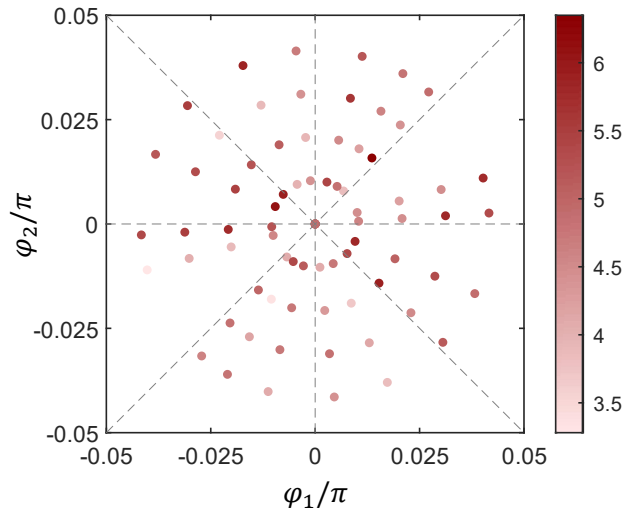


FIG. 3. Metrological gains for joint estimation of two spin rotations. The Metrological gain obtained from Eq. (4) with error propagation formulae  $\Delta\varphi_1 = \Delta Q_{yz} / |d\langle Q_{yz} \rangle / d\varphi_1|$  and  $\Delta\varphi_2 = \Delta Q_{xz} / |d\langle Q_{xz} \rangle / d\varphi_2|$ , where the denominators and numerators are obtained by fitting the measured spin-nematic operators  $\langle Q_{xz(yz)}^{\text{meas}} \rangle$  and  $\Delta Q_{xz(yz)}^{\text{meas}}$  using quartic functions without linear terms, respectively. Gains of 3.3 dB to 6.3 dB over the SQL are observed for  $\varphi_{1,2} \in [-0.05, 0.05]\pi$ .

Figure 2(c-f) show the parameter-dependent mean values and standard deviations of the measured  $Q_{yz}$  and  $Q_{xz}$ . Using the non-entangled polar state as the probe, the standard deviation observed is slightly higher than the shot noise as a result of technical imperfections of the pulses. For the spin-nematic squeezed state, the distributions of measured data are found squeezed along both the  $Q_{xz}$  and  $Q_{yz}$  axes. The mean values are linearly dependent on the parameter  $\alpha$  for fixed  $\Theta$ , while the standard deviations are almost independent of the parameters  $\alpha$  and  $\Theta$ . The measurement microwave pulses are generated by the same AWG (arbitrary waveform generator) as the phase imprinting RF pulses, which ensures a nearly perfect phase correlation between the two procedures. The total read-out protocol takes about 374  $\mu\text{s}$ , and during which the less-than-ideal differential phase shift between the two microwave signals also contributes to the phase noise, which altogether limits the measured squeezing and therefore the realized metrological gain. To further elucidate the performance of the joint estimation scheme, in Fig. 3, the metrological gain for the

two-phase estimation, defined as

$$\zeta = -10 \log_{10} \left[ \frac{(\Delta\varphi_1)^2 + (\Delta\varphi_2)^2}{(\Delta\varphi_1)_{\text{SQL}}^2 + (\Delta\varphi_2)_{\text{SQL}}^2} \right], \quad (4)$$

is shown in the rotation range of  $\varphi_{1,2} \in [-0.05, 0.05]\pi$  encoded to the spin-nematic squeezed probe state, enhancement of 3.3 dB to 6.3 dB beyond the SQL of 26000 atoms is observed. About 500 atoms are lost during the experiment cycle. We have also conducted an analysis of the metrological gain of the polar state and a sensitivity approximately 2 dB worse than the SQL is found, due to the crosstalk noise (See supplementary Material). The metrological gain is expected to be symmetric with respect to  $\varphi_1$  and  $\varphi_2$ , while the experimental results are affected by the pump phase noise (see Supplementary information) and degrade stochastically in the  $\varphi_1$ - $\varphi_2$  plane. Such degradation of metrological gain can be mitigated to some degree by carefully tuning the pump phase before sensing.

In conclusion, we propose and experimentally demonstrate, for the first time, the simultaneous estimation of two phases generated by two orthogonal (noncommuting) spin rotations using an entangled atomic ensemble. Sensitivities exceeding 3 dB beyond the standard quantum limit are observed across a wide range of rotation angles. By coherently coupling the atomic BEC in the ground  $F = 1$  manifold to the  $F = 2$  manifold, with the latter serving as the auxiliary field, and using a carefully designed microwave pulse sequence, simultaneous read-out of two noncommuting observables is realized. These observables serve as estimators for the broad range of parameters being measured. The metrological advantage of spin-nematic squeezed state was previously demonstrated in single-parameter estimation scenarios [41]. This work expands such quantum-enhanced sensing applications to multi-parameter quantum metrology and will likely stimulate the development of a broad range of application scenarios in atomic sensors. Limited by the coherence time of the spin-nematic squeezed state in our experiment, interaction-based readout, which recently enabled significantly enhanced metrological gains over direct linear read-out adopted here [41], remains to be implemented for studying the two-parameter estimation of this work. An operational protocol is known [33] and whose implementation will mitigate a large part of the atom number detection noise after coherence time is improved.

We thank Drs Q. Liu and L. N. Wu for helpful discussions. This work is supported by the National Key R&D Program of China (Grants No. 2018YFA0306504), by the National Natural Science Foundation of China (NSFC) (Grants No. 92265205 and No. U1930201), and by the Innovation Program for Quantum Science and Technology (2021ZD0302100).

J. C. and X. L. contributed equally to this work.

- 
- \* [xinwei.li1991@outlook.com](mailto:xinwei.li1991@outlook.com)  
† [lyou@tsinghua.edu.cn](mailto:lyou@tsinghua.edu.cn)
- [1] V. Giovannetti, S. Lloyd, and L. Maccone, Quantum-enhanced measurements: beating the standard quantum limit, *Science* **306**, 1330 (2004).
  - [2] V. Giovannetti, S. Lloyd, and L. Maccone, Advances in quantum metrology, *Nature photonics* **5**, 222 (2011).
  - [3] L. Pezzè, A. Smerzi, M. K. Oberthaler, R. Schmied, and P. Treutlein, Quantum metrology with nonclassical states of atomic ensembles, *Reviews of Modern Physics* **90**, 035005 (2018).
  - [4] C. M. Caves, Quantum-mechanical noise in an interferometer, *Physical Review D* **23**, 1693 (1981).
  - [5] J. Aasi, J. Abadie, B. Abbott, R. Abbott, T. Abbott, M. Abernathy, C. Adams, T. Adams, P. Addesso, R. Adhikari, *et al.*, Enhanced sensitivity of the ligo gravitational wave detector by using squeezed states of light, *Nature Photonics* **7**, 613 (2013).
  - [6] E. Polino, M. Valeri, N. Spagnolo, and F. Sciarrino, Photonic quantum metrology, *AVS Quantum Science* **2** (2020).
  - [7] X.-Y. Luo, Y.-Q. Zou, L.-N. Wu, Q. Liu, M.-F. Han, M. K. Tey, and L. You, Deterministic entanglement generation from driving through quantum phase transitions, *Science* **355**, 620 (2017).
  - [8] S. Colombo, E. Pedrozo-Peñañiel, A. F. Adiyatullin, Z. Li, E. Mendez, C. Shu, and V. Vuletić, Time-reversal-based quantum metrology with many-body entangled states, *Nature Physics* **18**, 925 (2022).
  - [9] K. A. Gilmore, M. Affolter, R. J. Lewis-Swan, D. Barberena, E. Jordan, A. M. Rey, and J. J. Bollinger, Quantum-enhanced sensing of displacements and electric fields with two-dimensional trapped-ion crystals, *Science* **373**, 673 (2021).
  - [10] C. D. Marciniak, T. Feldker, I. Pogorelov, R. Kaubruegger, D. V. Vasilyev, R. van Bijnen, P. Schindler, P. Zoller, R. Blatt, and T. Monz, Optimal metrology with programmable quantum sensors, *Nature* **603**, 604 (2022).
  - [11] W. Wang, Y. Wu, Y. Ma, W. Cai, L. Hu, X. Mu, Y. Xu, Z.-J. Chen, H. Wang, Y. Song, *et al.*, Heisenberg-limited single-mode quantum metrology in a superconducting circuit, *Nature Communications* **10**, 4382 (2019).
  - [12] E. Pedrozo-Peñañiel, S. Colombo, C. Shu, A. F. Adiyatullin, Z. Li, E. Mendez, B. Braverman, A. Kawasaki, D. Akamatsu, Y. Xiao, *et al.*, Entanglement on an optical atomic-clock transition, *Nature* **588**, 414 (2020).
  - [13] W. Muessel, H. Strobel, D. Linnemann, D. Hume, and M. Oberthaler, Scalable spin squeezing for quantum-enhanced magnetometry with bose-einstein condensates, *Physical Review Letters* **113**, 103004 (2014).
  - [14] M. Szczykulska, T. Baumgratz, and A. Datta, Multi-parameter quantum metrology, *Advances in Physics: X* **1**, 621 (2016).
  - [15] J. Liu, H. Yuan, X.-M. Lu, and X. Wang, Quantum fisher information matrix and multiparameter estimation, *Journal of Physics A: Mathematical and Theoretical* **53**, 023001 (2020).
  - [16] F. Albarelli, M. Barbieri, M. G. Genoni, and I. Gianani, A perspective on multiparameter quantum metrology: From theoretical tools to applications in quantum imaging, *Physics Letters A* **384**, 126311 (2020).
  - [17] E. Bisketzi, D. Branford, and A. Datta, Quantum limits of localisation microscopy, *New Journal of Physics* **21**, 123032 (2019).
  - [18] T. Baumgratz and A. Datta, Quantum enhanced estimation of a multidimensional field, *Physical Review Letters* **116**, 030801 (2016).
  - [19] X. Meng, Y. Zhang, X. Zhang, S. Jin, T. Wang, L. Jiang, L. Xiao, S. Jia, and Y. Xiao, Machine learning assisted vector atomic magnetometry, *Nature Communications* **14**, 6105 (2023).
  - [20] P. Komar, E. M. Kessler, M. Bishof, L. Jiang, A. S. Sørensen, J. Ye, and M. D. Lukin, A quantum network of clocks, *Nature Physics* **10**, 582 (2014).
  - [21] L. Pezzè, M. A. Ciampini, N. Spagnolo, P. C. Humphreys, A. Datta, I. A. Walmsley, M. Barbieri, F. Sciarrino, and A. Smerzi, Optimal measurements for simultaneous quantum estimation of multiple phases, *Physical Review Letters* **119**, 130504 (2017).
  - [22] L. O. Conlon, T. Vogl, C. D. Marciniak, I. Pogorelov, S. K. Yung, F. Eilenberger, D. W. Berry, F. S. Santana, R. Blatt, T. Monz, *et al.*, Approaching optimal entangling collective measurements on quantum computing platforms, *Nature Physics* **19**, 351 (2023).
  - [23] S. L. Braunstein and H. J. Kimble, Dense coding for continuous variables, *Physical Review A* **61**, 042302 (2000).
  - [24] X. Li, Q. Pan, J. Jing, J. Zhang, C. Xie, and K. Peng, Quantum dense coding exploiting a bright einstein-podolsky-rosen beam, *Physical Review Letters* **88**, 047904 (2002).
  - [25] S. Steinlechner, J. Bauchrowitz, M. Meinders, H. Müller-Ebhardt, K. Danzmann, and R. Schnabel, Quantum-dense metrology, *Nature Photonics* **7**, 626 (2013).
  - [26] Y. Liu, J. Li, L. Cui, N. Huo, S. M. Assad, X. Li, and Z. Ou, Loss-tolerant quantum dense metrology with su(1,1) interferometer, *Optics Express* **26**, 27705 (2018).
  - [27] W. Du, J. Chen, Z. Ou, and W. Zhang, Quantum dense metrology by an su(2)-in-su(1,1) nested interferometer, *Applied Physics Letters* **117** (2020).
  - [28] The USTC/CUHK paper *Multi-parameter quantum metrology with stabilized multi-mode squeezed state*. While our work is being prepared for publication, we become aware of this related study on squeezed center-of-mass motion of a trapped ion in two orthogonal directions.
  - [29] The University of Oregon paper with Two-mode squeezing and SU(1,1) interferometry with trapped ions. While our work is being prepared for publication, we notice this related study on generation of two-mode squeezed state with trapped ions and demonstration of SU(1,1) interferometers.
  - [30] C. Gross, H. Strobel, E. Nicklas, T. Zibold, N. Bar-Gill, G. Kurizki, and M. Oberthaler, Atomic homodyne detection of continuous-variable entangled twin-atom states, *Nature* **480**, 219 (2011).
  - [31] C. D. Hamley, C. Gerving, T. Hoang, E. Bookjans, and M. S. Chapman, Spin-nematic squeezed vacuum in a quantum gas, *Nature Physics* **8**, 305 (2012).
  - [32] J. Peise, I. Kruse, K. Lange, B. Lücke, L. Pezzè, J. Arlt, W. Ertmer, K. Hammerer, L. Santos, A. Smerzi, *et al.*, Satisfying the einstein-podolsky-rosen criterion with massive particles, *Nature Communications* **6**, 8984 (2015).
  - [33] X. Li, *Quantum enhanced metrology for simultaneous multiparameter estimation*, Ph.D. thesis, Tsinghua Uni-

- versity (2021).
- [34] Q. Liu, L.-N. Wu, J.-H. Cao, T.-W. Mao, X.-W. Li, S.-F. Guo, M. K. Tey, and L. You, Nonlinear interferometry beyond classical limit enabled by cyclic dynamics, *Nature Physics* **18**, 167 (2022).
  - [35] C. S. Jackson and C. M. Caves, Simultaneous measurements of noncommuting observables: Positive transformations and instrumental lie groups, *Entropy* **25**, 1254 (2023).
  - [36] C. Law, H. Pu, and N. Bigelow, Quantum spins mixing in spinor bose-einstein condensates, *Physical Review Letters* **81**, 5257 (1998).
  - [37] F. Gerbier, A. Widera, S. Fölling, O. Mandel, and I. Bloch, Resonant control of spin dynamics in ultracold quantum gases by microwave dressing, *Physical Review A* **73**, 041602 (2006).
  - [38] D. Linnemann, H. Strobel, W. Muessel, J. Schulz, R. J. Lewis-Swan, K. V. Kheruntsyan, and M. K. Oberthaler, Quantum-enhanced sensing based on time reversal of nonlinear dynamics, *Physical Review Letters* **117**, 013001 (2016).
  - [39] D. Walls and G. J. Milburn, Input–output formulation of optical cavities, in *Quantum optics* (Springer, 2008) pp. 127–141.
  - [40] P. Kunkel, M. Prüfer, S. Lannig, R. Rosa-Medina, A. Bonnin, M. Gärttner, H. Strobel, and M. K. Oberthaler, Simultaneous readout of noncommuting collective spin observables beyond the standard quantum limit, *Physical Review Letters* **123**, 063603 (2019).
  - [41] T.-W. Mao, Q. Liu, X.-W. Li, J.-H. Cao, F. Chen, W.-X. Xu, M. K. Tey, Y.-X. Huang, and L. You, Quantum-enhanced sensing by echoing spin-nematic squeezing in atomic bose–einstein condensate, *Nature Physics* (2023), <https://doi.org/10.1038/s41567-023-02168-3>.
  - [42] C. Gardiner and P. Zoller, *Quantum noise: a handbook of Markovian and non-Markovian quantum stochastic methods with applications to quantum optics* (Springer Science & Business Media, 2004).
  - [43] P. B. Blakie, A. Bradley, M. Davis, R. Ballagh, and C. Gardiner, Dynamics and statistical mechanics of ultracold bose gases using c-field techniques, *Advances in Physics* **57**, 363 (2008).

## Supplemental Material for: Joint estimation of a two-phase spin rotation beyond classical limit

### SPIN-NEMATIC SQUEEZING IN SPIN-1 SYSTEM

#### Dynamical simulations

For a spin-1 Bose-Einstein condensate (BEC) composed of  $N$   $^{87}\text{Rb}$  atoms, the full spin-mixing dynamics under single spatial mode approximation (SMA) [36] is described by the following Hamiltonian

$$H = \frac{c_2}{2N} [2(a_1^\dagger a_{-1}^\dagger a_0 a_0 + a_1 a_{-1} a_0^\dagger a_0^\dagger) + (N_1 - N_{-1})^2 + (2N_0 - 1)(N_1 + N_{-1})] - qN_0, \quad (\text{S1})$$

where  $c_2 < 0$  is the ferromagnetic spin-exchange interaction coefficient, and  $q$  is the quadratic Zeeman shift (QZS).  $a_m$  ( $a_m^\dagger$ ) is the annihilation (creation) operator for atoms in the  $|F = 1, m = \{0, \pm 1\}\rangle$  spin component and  $N_m = a_m^\dagger a_m$  represents the associated atom number. To realistically simulate the generation of the spin-

nematic squeezing in experiments, it is necessary to take into account atom loss, and the spin-mixing dynamics can then be modeled by the master equation

$$\frac{d\rho}{dt} = -i[H(t), \rho] + \sum_{m=0, \pm 1} \gamma_m \mathcal{D}[a_m] \rho, \quad (\text{S2})$$

where  $\mathcal{D}[a_m]\rho = a_m \rho a_m^\dagger - \{a_m^\dagger a_m, \rho\}/2$  accounts for atom loss with dissipative rate  $\gamma_m$  for the  $|F = 1, m\rangle$  component. Here we assume  $\gamma_m = \gamma$  for  $m = 0, \pm 1$ , and  $H(t)$  is a time-dependent Hamiltonian obtained after replacing  $N$  and  $c_2$  in Eq. (S1) by  $N(t) = Ne^{-\gamma t}$  and  $c_2(t) = c_2 e^{-\gamma_c t}$ , where  $\gamma_c$  is the decay rate of  $c_2$ .

The above master equation can be numerically simulated with the semiclassical truncated Wigner method (TWM) [42, 43], which maps the field operators  $a_m$  and  $a_m^\dagger$  into complex numbers  $\psi_m$  and  $\psi_m^*$  with the time evolution of the system unraveled into a set of stochastic differential equations (SDEs) as given in the following

$$\begin{aligned} d\psi_1 &= -ic_2' [\psi_0^2 \psi_{-1}^* + (|\psi_1|^2 - |\psi_{-1}|^2 + |\psi_0|^2) \psi_1] dt - \frac{\gamma}{2} \psi_1 dt + \sqrt{\frac{\gamma}{2}} d\xi_1(t), \\ d\psi_0 &= -ic_2' [2\psi_1 \psi_{-1} \psi_0^* + (|\psi_1|^2 + |\psi_{-1}|^2) \psi_0] dt + iq\psi_0 dt - \frac{\gamma}{2} \psi_0 dt + \sqrt{\frac{\gamma}{2}} d\xi_0(t), \\ d\psi_{-1} &= -ic_2' [\psi_0^2 \psi_1^* + (|\psi_{-1}|^2 - |\psi_1|^2 + |\psi_0|^2) \psi_{-1}] dt - \frac{\gamma}{2} \psi_{-1} dt + \sqrt{\frac{\gamma}{2}} d\xi_{-1}(t). \end{aligned} \quad (\text{S3})$$

In the above,  $c_2' = c_2(t)/N(t)$  denotes the drifting spin-exchange rate in the presence of atom loss.  $d\xi_m(t)$  represents a complex Wiener noise increment satisfying  $\overline{d\xi_m(t)} = 0$ ,  $\overline{d\xi_m^*(t) d\xi_n(t)} = \delta_{m,n} dt$ . The SDEs are capable of describing quantum evolution of the Master Eq. (S2) after averaged over an ensemble of trajectories. The effect of quantum noise is incorporated into the probability distribution of the initial polar state, which is given by the Wigner function and can be sampled according to

$$\begin{aligned} \psi_{\pm 1} &= \frac{1}{2}(\alpha_{\pm 1} + i\beta_{\pm 1}), \\ \psi_0 &= \sqrt{N} + \frac{1}{2}(\alpha_{\pm 0} + i\beta_{\pm 0}), \end{aligned} \quad (\text{S4})$$

where  $\alpha_m$  and  $\beta_m$  are independent real numbers following a standard normal distribution. The averages and variances of mode populations are then obtained from the averages of 10000 simulated trajectories, calculated according to  $\langle \hat{N}_m \rangle = \overline{\psi_m^* \psi_m} - 1/2$  and  $\langle \Delta \hat{N}_m \rangle^2 = \langle \Delta \psi_m^* \psi_m \rangle^2 - 1/4$ .

The parameters used in our simulations include initial

atom number  $N = 26000$ ,  $c_2 = -2\pi \times 3.8$  Hz,  $q = 2\pi \times 3.9$  Hz, and loss rate  $\gamma = 0.069$  s $^{-1}$ , all of which are independently calibrated in experiments. We also experimentally compensate for the influence of atom loss by ramping  $q$  with a rate  $\gamma_q = \gamma_c$  to keep  $c_2(t)/q(t)$  fixed as in Refs. [34, 41].

#### SU(3) operators and Bloch spheres

To better understand the spin-mixing dynamics in phase space, both the angular momentum  $L_i$  and the nematic tensor  $Q_{i,j}$  ( $i, j \in x, y, z$ ) operators, which constitute SU(3) Lie algebra, are needed. The definition of

the nematic tensor operators are as follows

$$\begin{aligned}
Q_{yz} &= \frac{i}{\sqrt{2}} \left( -a_1^\dagger a_0 + a_0^\dagger a_1 - a_{-1}^\dagger a_0 + a_0^\dagger a_{-1} \right), \\
Q_{xz} &= \frac{1}{\sqrt{2}} \left( a_1^\dagger a_0 + a_0^\dagger a_1 - a_{-1}^\dagger a_0 - a_0^\dagger a_{-1} \right), \\
Q_{xx} &= \frac{2}{3} a_0^\dagger a_0 - \frac{1}{3} a_1^\dagger a_{-1} - \frac{1}{3} a_{-1}^\dagger a_{-1} + a_{-1}^\dagger a_1 + a_1^\dagger a_{-1}, \\
Q_{yy} &= \frac{2}{3} a_0^\dagger a_0 - \frac{1}{3} a_1^\dagger a_{-1} - \frac{1}{3} a_{-1}^\dagger a_{-1} - \hat{a}_{-1}^\dagger a_1 - a_1^\dagger a_{-1}, \\
Q_{zz} &= \frac{2}{3} a_1^\dagger a_1 - \frac{4}{3} a_0^\dagger a_0 + \frac{2}{3} a_{-1}^\dagger a_{-1},
\end{aligned} \tag{S5}$$

and the spin-1 angular momentum operators are

$$\begin{aligned}
L_x &= \frac{1}{\sqrt{2}} \left( a_1^\dagger a_0 + a_0^\dagger a_1 + a_{-1}^\dagger a_0 + a_0^\dagger a_{-1} \right), \\
L_y &= \frac{i}{\sqrt{2}} \left( -a_1^\dagger a_0 - a_0^\dagger a_{-1} + a_0^\dagger a_1 + a_{-1}^\dagger a_0 \right), \\
L_z &= a_1^\dagger a_1 - a_{-1}^\dagger a_{-1}.
\end{aligned} \tag{S6}$$

The above eight operators are linearly independent, and they form seven triple operator combinations that span SU(2) subspaces. The spin-nematic squeezing can be illustrated in the subspace Bloch spheres formed by  $\{Q_{yz}, L_x, (Q_{yy} - Q_{zz})/2\}$  and  $\{L_y, Q_{xz}, (Q_{xx} - Q_{zz})/2\}$  as shown in the main text.

## SIMULTANEOUS MEASUREMENTS OF $Q_{xz}$ AND $Q_{yz}$

### Quadrature squeezing and atomic homodyne detection

For the short-time evolution starting from polar state, atom number in the  $|F = 1, m = 0\rangle$  component is approximately undepleted. At  $q = |c_2|$ , the complete Hamiltonian approximately takes the two-mode squeezing form after the replacement  $\hat{a}_0^\dagger \rightarrow \sqrt{N}e^{i\phi_0}$

$$H_{\text{udp}} = c_2(e^{2i\phi_0} a_1 a_{-1} + e^{-2i\phi_0} a_1^\dagger a_{-1}^\dagger), \tag{S7}$$

with  $\phi_0 = 0$ . Equation (S7) thus gives the equivalent two-mode squeezing dynamics as in undepleted pump optical four-wave mixing (FWM) or parametric down conversion, and the angular momentum operators  $L_x$  and  $L_y$  as well as the nematic tensor operators  $Q_{yz}$  and  $Q_{xz}$  all reduce to quadrature operators

$$\begin{aligned}
L_x &= \sqrt{\frac{N}{2}} [(a_{+1}^\dagger + a_{-1}^\dagger) + (a_{+1} + a_{-1})], \\
L_y &= i\sqrt{\frac{N}{2}} [(a_{-1}^\dagger - a_{+1}^\dagger) + (a_{+1} - a_{-1})], \\
Q_{yz} &= -i\sqrt{\frac{N}{2}} [(a_{+1}^\dagger + a_{-1}^\dagger) - (a_{+1} + a_{-1})], \\
Q_{xz} &= \sqrt{\frac{N}{2}} [(a_{+1}^\dagger - a_{-1}^\dagger) + (a_{+1} - a_{-1})].
\end{aligned} \tag{S8}$$

It is then straightforward to see that  $Q_{yz}$  and  $Q_{xz}$  can be measured following atomic homodyne detection [30] with two coherent pumps of a relative  $\pi/2$  phase difference.

In the simultaneous measurement scheme adopted for our experiment as depicted in Fig. 1(c) of the main text, the first three steps execute the transformation of

$$\begin{aligned}
a'_{1,-1} &= \frac{1}{\sqrt{2}} a_{1,+1} + \frac{1}{\sqrt{2}} a_{1,-1} = a_S, \\
a'_{1,+1} &= \frac{1}{\sqrt{2}} a_{1,+1} - \frac{1}{\sqrt{2}} a_{1,-1} = a_A,
\end{aligned} \tag{S9}$$

and split atoms in the  $|F = 1, m = 0\rangle$  component into two halves

$$\begin{aligned}
a'_{2,-1} &= i\varepsilon_1 a_{1,0}, \\
a'_{2,+1} &= \varepsilon_2 a_{1,0}.
\end{aligned} \tag{S10}$$

Here for simplicity, we take  $\varepsilon_1 \approx \varepsilon_2 \approx 1/\sqrt{2}$ , while in realistic experiments a small number of atoms (less than 1000) could remain in the  $|F = 1, m = 0\rangle$  component, which can be neglected as the population of the pump is relatively large.

The fourth step coupling the signals  $a_S$  and  $a_A$  to the coherent pump enable atomic homodyne detection simultaneously. After the MW pulse, we obtain

$$\begin{aligned}
a_{2,-2}^{\text{out}} &= \frac{1}{\sqrt{2}} \left( \frac{1}{\sqrt{2}} a_{1,+1} + \frac{1}{\sqrt{2}} a_{1,-1} + i\varepsilon_1 a_{1,0} \right), \\
a_{2,-1}^{\text{out}} &= \frac{1}{\sqrt{2}} \left( \frac{i}{\sqrt{2}} a_{1,+1} + \frac{i}{\sqrt{2}} a_{1,-1} + \varepsilon_1 a_{1,0} \right), \\
a_{2,+2}^{\text{out}} &= \frac{1}{\sqrt{2}} \left( \frac{1}{\sqrt{2}} a_{1,+1} - \frac{1}{\sqrt{2}} a_{1,-1} - \varepsilon_2 a_{1,0} \right), \\
a_{2,+1}^{\text{out}} &= \frac{1}{\sqrt{2}} \left( \frac{1}{\sqrt{2}} a_{1,+1} - \frac{1}{\sqrt{2}} a_{1,-1} + \varepsilon_2 a_{1,0} \right),
\end{aligned} \tag{S11}$$

with the final step transferring atoms in  $|F = 1, m = 1\rangle$  and  $|F = 1, m = -1\rangle$  into  $|F = 2, m = 1\rangle$  and  $|F = 2, m = -1\rangle$  components respectively. The populations in the above  $F = 2$  components can be detected simultaneously from absorption imaging of the  $F = 1$  components. Using Eq. (S11), we obtain  $Q_{xz}$  and  $Q_{yz}$  in a single experimental run according to

$$\begin{aligned}
N_{2,-1}^{\text{out}} - N_{1,-1}^{\text{out}} &= \frac{i\varepsilon_1}{\sqrt{2}} (a_{1,0}^\dagger a_{1,+1} + a_{1,0}^\dagger a_{1,-1}) + \text{H.c.} = \varepsilon_1 Q_{yz}, \\
N_{2,+1}^{\text{out}} - N_{1,+1}^{\text{out}} &= \frac{\varepsilon_2}{\sqrt{2}} (a_{1,+1}^\dagger a_{1,0} - a_{1,-1}^\dagger a_{1,0}) + \text{H.c.} = \varepsilon_2 Q_{xz}.
\end{aligned} \tag{S12}$$

### Influence of crosstalk between the pump and the signal

The first three steps of the measurement scheme split the pump mode  $a_{1,0}$  into two halves and establish a  $\pi/2$  SU(2) rotation between  $a_{1,1}$  and  $a_{1,-1}$ . In the ideal scenario, the signals are not affected by pumps as their

polarizations are orthogonal. The unwanted couplings are, however, inevitable between sublevels of  $F = 1$  and  $F = 2$ , hence they introduce noise into the signal modes. Such imperfection degrades the simultaneously measured squeezing in both subspaces, and whose influence can be simulated by adding Gaussian distributed noise to the signal modes according to

$$\begin{aligned} a_S &= \frac{1}{\sqrt{2}}a_{1,+1} + \frac{1}{\sqrt{2}}a_{1,-1} + \eta_S, \\ a_A &= \frac{1}{\sqrt{2}}a_{1,+1} - \frac{1}{\sqrt{2}}a_{1,-1} + \eta_A, \end{aligned} \quad (\text{S13})$$

where  $\eta_S$  and  $\eta_A$  represent complex sources of white noise satisfying  $\langle \eta_S \rangle = \langle \eta_A \rangle = 0$  and  $\langle \eta_S^2 \rangle = \langle \eta_A^2 \rangle = 1$ . The noise strength for  $a_S$  and  $a_A$  are assumed to be equal  $\delta\eta_S = \delta\eta_A = \delta\eta$  for simplicity here.

To calibrate the strength of the noise  $\delta\eta$ , we perform numerical calculations to assess the fluctuations of the simultaneously measured  $Q_{yz}$  and  $Q_{xz}$  for polar state, which remains unaffected by pump phase noise. Figure S1 illustrates a comparison between the experimental results and our numerical simulations, which reveals a value of approximately  $\delta\eta = 0.3$ . It is worth pointing out that our numerical simulations incorporate a calibrated detection noise of  $\Delta(N_{2,\pm 1}^{\text{out}} - N_{1,\pm 1}^{\text{out}}) = 24$  in the atomic population difference.

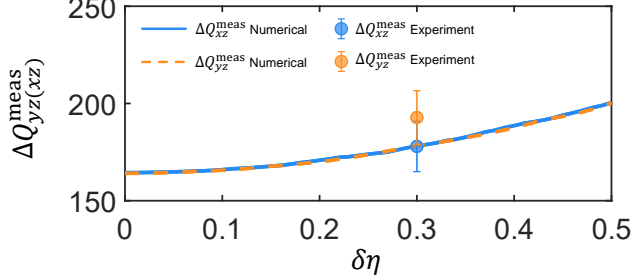


FIG. S1. Calibration of the signal-pump crosstalk noise strength with polar state. The blue solid line represents the numerical simulations of  $\Delta Q_{xz}^{\text{meas}}$  as a function of the crosstalk noise strength, while the orange color dashed line corresponds to that of  $\Delta Q_{yz}^{\text{meas}}$ . The experimental results are depicted by the blue and orange dots, which align reasonably close with the corresponding numerical simulations at  $\delta\eta \approx 0.3$ .

### Influence of pump phase noise

When measuring squeezing in both subspaces, the phases of the two coherent pumps are required to differ by  $\pi/2$ . Due to the imperfection of MW pulses, fluctuation of the pump phase needs to be considered as well. While the polar state is insensitive to this noise, spin-nematic squeezed state is extremely sensitive to it, which

can be modeled by adding Gaussian distributed random phase into the pump mode

$$\begin{aligned} a_{2,-2}^{\text{out}} &= \frac{1}{\sqrt{2}}(a_S + i\varepsilon_1 e^{i\theta_1} a_{1,0}), \\ a_{2,-1}^{\text{out}} &= \frac{1}{\sqrt{2}}(ia_S + \varepsilon_1 e^{i\theta_1} a_{1,0}), \\ a_{2,+2}^{\text{out}} &= \frac{1}{\sqrt{2}}(a_A - \varepsilon_2 e^{i\theta_2} a_{1,0}), \\ a_{2,+1}^{\text{out}} &= \frac{1}{\sqrt{2}}(a_A + \varepsilon_2 e^{i\theta_2} a_{1,0}). \end{aligned} \quad (\text{S14})$$

Here we assume  $\delta\theta_1 = \delta\theta_2 = \delta\theta$  for simplicity. To calibrate the noise strength, we numerically calculate the fluctuations of the simultaneously measured  $Q_{yz}$  and  $Q_{xz}$  for the spin-nematic squeezed state. As shown in Fig. S2, our numerical simulations corroborate well with experimental results at  $\delta\theta \approx 0.0075 \times 2\pi$ .

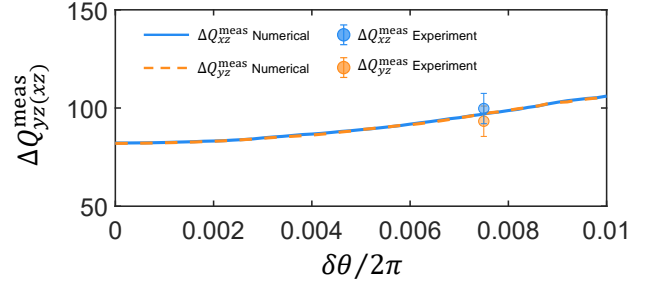


FIG. S2. Calibration of the pump phase noise strength with spin-nematic squeezed state. The blue solid line represents the numerical simulation of  $\Delta Q_{xz}^{\text{meas}}$  as a function of the pump phase noise strength, while the orange dashed line corresponds to that of  $\Delta Q_{yz}^{\text{meas}}$ . The experimental results are depicted by the blue and orange dots, which align closely with the corresponding numerical simulations at  $\delta\theta \approx 0.0075 \times 2\pi$ .

## ANALYSIS OF THE METROLOGICAL GAIN

### Sensitivity

We employ the error propagation formula to analyze the phase sensitivity of our joint parameter estimation protocol. The sensitivities of  $\varphi_1$  and  $\varphi_2$  can be obtained with

$$\begin{aligned} \Delta\varphi_1 &= \frac{\Delta Q_{yz}}{\delta \langle Q_{yz} \rangle / \delta\varphi_1} = \frac{\Delta Q_{yz}}{\delta \langle Q_{yz} \rangle / [(\cos \Theta)\delta\alpha + \alpha(\sin \Theta)\delta\Theta]}, \\ \Delta\varphi_2 &= \frac{\Delta Q_{xz}}{\delta \langle Q_{xz} \rangle / \delta\varphi_2} = \frac{\Delta Q_{xz}}{\delta \langle Q_{xz} \rangle / [(\sin \Theta)\delta\alpha + \alpha(\cos \Theta)\delta\Theta]}. \end{aligned} \quad (\text{S15})$$

### Standard quantum limit of joint parameter estimation

The quantum metrological gain for parameter estimation protocol is customarily discussed with respect to its classical reference, the standard quantum limit (SQL), which is defined as the optimal phase sensitivity that can be achieved without quantum entanglement. When the unentangled polar state is employed as the probe, the sensitivity for a single parameter estimation is given by

$$\Delta\varphi_{\text{SQL}} = \frac{1}{2\sqrt{N}}, \quad (\text{S16})$$

where the factor of 2 arises from the presence of three interference modes. In the present work, two phases are estimated simultaneously, leading to the SQL as

$$\Delta\vec{\varphi}_{\text{SQL}} = \sqrt{(\Delta\varphi_{1,\text{SQL}})^2 + (\Delta\varphi_{2,\text{SQL}})^2} = \frac{1}{\sqrt{2N}}. \quad (\text{S17})$$

## EXPERIMENTAL METHODS

### Initial state preparation

We prepare an initial state with about 26500  $^{87}\text{Rb}$  atoms condensed in the ground  $|F=1, m_F=0\rangle$  hyperfine state, confined in a crossed dipole trap with trapping frequencies around  $2\pi \times (190, 90, 120)$  Hz along three orthogonal directions, by first removing atoms occupying the other states with a gradient magnetic field. The bias magnetic field is set at 0.838 G, which offers a quadratic magnetic Zeeman shift of  $q_B \approx 2\pi \times 50$  Hz =  $13|c_2|$  to inhibit spin-mixing. To further purify the initial polar state, two resonant microwave pulses coupling  $|F=1, m_F=\pm 1\rangle$  to  $|F=2, m_F=\pm 2\rangle$  are applied, followed by a probe light pulse beam to flush away the remaining  $|\pm 1\rangle$  atoms. Subsequent spin-mixing evolution is initiated by switching on a microwave dressing field 12.18 MHz blue-detuned from the  $|1, 0\rangle$  to  $|2, 0\rangle$  transition, quenching  $q$  from  $13|c_2|$  to near  $|c_2|$ .

### Microwave pulse synthesizing

During the experiment, a sequence of phase-coherent microwave pulses with controllable  $\sigma_{+/-}$ -polarization is needed. It is synthesized by combining a microwave signal generator (SMB100A) with output frequency set at 6.6 GHz, and a four-channel AWG (DN2.663-04), output set at 200 MHz, using a Mini-Circuits mixer. The power stabilization is achieved by a power feedback loop. The polarization control is achieved by adjusting the relative phase between the two microwave antennas, which are placed along different spatial directions, hence carrying different polarization components. The signals of

the two antennas are generated from two AWG channels, thus they remain phase coherent.

### Calibration of atom number detection

The detection signal comes from absorption imaging, therefore the detected atom number accuracy is of great importance to the measurement. We prepare initial polar states with all atoms in  $|F=1, m_F=0\rangle$  at different numbers, then apply a resonant RF  $\pi/2$  pulse to generate coherent spin state  $(|+1\rangle + |-1\rangle)^{\otimes N}/2^{N/2}$  and measure the variance of number difference between  $|1, \pm 1\rangle$  states. As shown in Fig. S3, we find the number difference variance matches with that of the coherent state projection noise, which affirms the detection accuracy.

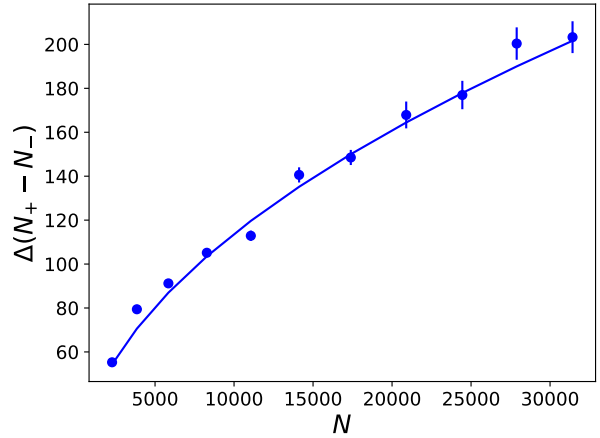


FIG. S3. Calibration of the atom number detection accuracy. The solid line denotes  $\sqrt{N}$ , the theoretical number difference variance of the coherent state. The blue dots show the measured variance, which match well with the solid line, affirming the accuracy of atom number detection.

### RF amplitude calibration

The small angle RF rotation is carried out by two resonant RF pulses with  $\pi$  phase difference, and the rotation angle is adjusted by changing pulse duration. We prepare the coherent state  $(-i|+1\rangle + \sqrt{2}|0\rangle - i|-1\rangle)^{\otimes N}/2^{N/2}$  with  $\langle\rho_0\rangle = 1/2$  by RF rotation applied to the initial polar state. Subsequently, a small-angle RF rotation is applied along the same axis, resulting in a change in  $\langle\rho_0\rangle$  proportional to the rotation angle  $\alpha$ , expressed as  $\langle\rho_0\rangle = 1/2 + \alpha$  for small values of  $\alpha$ . The population changes with different pulse duration, providing a linear calibration to the rotation angle, as shown in Fig. S4.

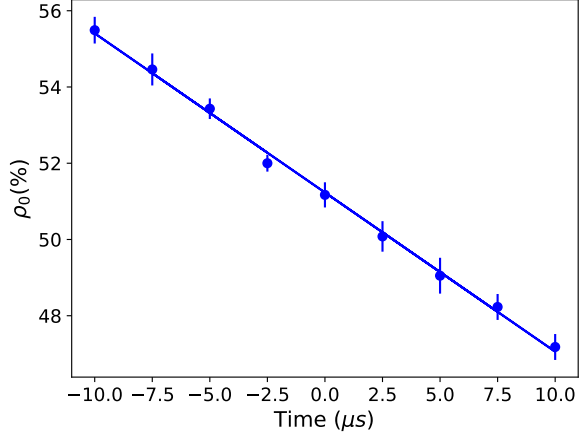


FIG. S4. The calibration of RF rotation angle. We use two resonant RF pulses with  $\pi$  phase difference to realize small angle rotation. The rotation angle is adjusted by fixing one pulse and changing the duration of the other. The blue dots show the measured  $\langle \rho_0 \rangle$  changes for coherent state  $(-i|+1\rangle + \sqrt{2}|0\rangle - i|-1\rangle)^{\otimes N} / 2^N$  under such rotations, and the solid line depicts a linear fit of the measured data.